RSC Advances



PAPER View Article Online



Cite this: RSC Adv., 2019, 9, 39622

Dendritic fibrous nano-silica & titania (DFNST) spheres as novel cataluminescence sensing materials for the detection of diethyl ether†

Yabin Wang, (1) ‡** Keke Hu, ‡* Yantu Zhang* and Xiuping Ding*

Selective and controllable cataluminescence (CTL) sensors for volatile organic compounds (VOCs) are significant for chemical safety, environmental monitoring, health effects on human beings, and so forth. Most of the exploited CTL-based sensors suffer relatively low response and poor selectivity because of their high sensitivities to interferential substances. In this investigation, dendritic fibrous nano-silica & titania (DFNST) spheres have been synthesized as novel sensing materials and the corresponding DFNSTbased CTL sensor has been fabricated to detect diethyl ether with high selectivity via a method of utilizing one 440 nm bandpass filter. The as-prepared DFNST hybrids not only keep the excellent dendritic fibrous morphology but also bear ca. 21 wt% catalytic titanium oxide of anatase crystalline structure. The DFNST-based sensor exhibits extremely strong CTL emission at 440 nm toward diethyl ether against other VOCs like acetone, ethyl acetate, butanol, and so forth. The high response can be attributed to the unique architectural texture of DFNST. Under the optimum parameters, ether could be easily detected in a wide range from 2.0 to 40.0 mM with a fine detection limit of 1.55 mM (S/N = 3). Furthermore, the working life of this CTL sensor is satisfactory with outstanding stability and durability, far from damaging the morphology and activity of the DFNST sensing material. In conclusion, it is expected that this novel sensing material, the relevant CTL sensor, and the approach of employing the bandpass filter will be significant for the detection of diethyl ether in actual applications.

Received 8th October 2019 Accepted 25th November 2019

DOI: 10.1039/c9ra08152f

rsc.li/rsc-advances

Introduction

Detrimental volatile organic compounds (VOCs) can lead to short- or long-term potential health effects on human beings. In the past few decades, multitudinous measuring techniques were explored to detect and discriminate hazardous chemicals in VOCs, such as inductively coupled plasma mass spectrometry (ICP-MS), gas chromatography mass spectrometry (GC-MS), and gas sensors. ¹⁻⁶ Among these techniques, gas sensors are deemed to be promising because of their high sensitivity, long-term stability, and the simplicity of the apparatus. Cataluminescence (CTL)-based sensors, as one type of gas sensors, possess further excellent detection advantages of rapid response, high signal/noise ratio (S/N), stable and durable intensity, *etc.* ^{2,3,7} In short, CTL-based sensors provide a versatile path for VOCs differentiation.

Diethyl ether as one of the harmful VOCs has posed a threat on human health and environmental security, owing to its flammable and explosive characters. As a consequence, it is imperative to detect diethyl ether in medicine, laboratory or industry applications. Considerable advances have been made in CTL-based sensors for diethyl ether detection, especially the utilized sensing materials. For example, Li's team fabricated core-shell Fe₃O₄@SiO₂ microspheres and applied them to detect diethyl ether.8 Under the optimal conditions, the system could achieve a detection range of 10-3000 ppm and own the detection limit of about 6.7 ppm. Lu et al. employed mesoporous TiO₂ nanoparticles as the catalytic material and solely diethyl ether displayed strong CTL emission at 440 nm in a range of 2.0 to 50.0 mM.2 Very recently, Zhen and coworkers used α-MoO₃ nanobelts as the sensing material for ether detection. The α-MoO₃ sensor brought about a lower detection temperature at 120 °C with a wide detection range of 9-2000 ppm and a low detection limit of about 7.5 ppm.9 From the above investigations, it can be concluded that nanomaterials have unique advantages as the sensing materials to fabricate CTL sensors because of their unique structural characteristics, like large surface areas and numerous active sites.

As introduced and classified in our previous work, ¹⁰ dendritic fibrous nano-particles (DFNPs) possess three-dimensional (3D) center-radial nanochannels along with

[&]quot;Shaanxi Key Laboratory of Chemical Reaction Engineering, College of Chemistry and Chemical Engineering, Yan'an University, Yan'an 716000, Shaanxi, P. R. China. E-mail: ybw_bingerbingo@126.com

^bKey Laboratory of Comprehensive and Highly Efficient Utilization of Salt Lake Resources, Salt Lake Chemistry Analysis and Test Center, Qinghai Institute of Salt Lakes, Chinese Academy of Sciences, Xining 810008, P. R. China

[†] Electronic supplementary information (ESI) available. See DOI: 10.1039/c9ra08152f ‡ These authors contributed equally to this work.

RSC Advances Paper

hierarchical nanopores (Fig. 1a) that give rise to larger pore volume and specific surface area, compared with most of traditional mesoporous materials like MCM-41 and SBA-15. DFNPs family can be divided into the pure ones (silica-, carbon-, titania-, etc.) and the hybrid like nano-silica & titania. However, up to now, only silica-based DFNPs (dendritic fibrous nano-silica, DFNS)10-16 have drawn considerable attention and undergone speedy development. It is worth to mention that DFNS was originally denominated and well-known as KCC-1.17-26 As DFNS subject boomingly developed, the idea of preparing dendritic fibrous nano-silica & titania (DFNST) naturally showed up, owing to the particular optical and electronic properties of titania (TiO₂). Our team and some other groups have proposed to manufacture DFNST hybrid with DFNS as hard template by the post-grafting method. 10,27-29

In this work, we first prepared DFNST nanospheres by grafting TBOT onto DFNS surfaces as demonstrated in Fig. 1b. The asprepared products not only keep the excellent dendritic fibrous topology but also bear ca. 21 wt% titanium oxide of anatase crystalline structure. The architecture and fundamental physicochemical properties were probed into by SEM, TEM, X-ray diffraction (XRD), X-ray photoelectron spectroscopy (XPS), inductively coupled plasma optical emission spectrometry (ICP-OES), N2 adsorption-desorption isotherms, Fourier transform infrared spectroscopy (FT-IR), and Raman spectrum. Secondly, for the first time, the as-prepared DFNST photocatalysts were pioneeringly applied as the sensing materials for the detection of diethyl ether via CTL (Fig. 1c). Highly selective detection was controllable and

realized by locating the detection position at 440 nm via one wavelength bandpass filter. Under the optimal parameters, DFNSTbased sensor could identify diethyl ether in a range of 2.0-40.0 mM with a detection limit of 1.55 mM (S/N = 3). Finally, the plausible CTL mechanism was proposed and discussed.

Experimental details

Chemicals

Tetraethylorthosilicate (TEOS), tetrabutyl orthotitanate (TBOT), cetylpyridinium bromide (CPB), ammonium hydroxide (NH₃·H₂O), urea, cyclohexane, pentanol, ethyl alcohol, and diethyl ether were purchased from Aladdin Corporation.

Synthesis processes

DFNS synthesis. DFNS was fabricated by a one-pot rotating hydrothermal technique via a JX-8-200 homogeneous reactor (China) with a certain stirring rate as reported in our previous work.10,30 Tetraethyl orthosilicate (TEOS, 2.5 g, 0.012 mol) was dissolved in a mixed cyclohexane (30 mL) and pentanol (1.5 mL). Another solution of urea (0.6 g, 0.01 mol) and cetylpyridinium bromide (CPB, 1 g, 0.0026 mol) in water (30 g, 1.67 mol) was poured into the above organic solution. The mixture solution was stirred for 60 min at 25 °C and then placed in an autoclave. Then, the autoclave was heated at 120 °C for 4 h with a stirring rate of 60 revolutions per minute (rpm). Finally, the product was centrifugated, washed with acetone for six times, and calcined at 550 °C for 6 h, respectively.

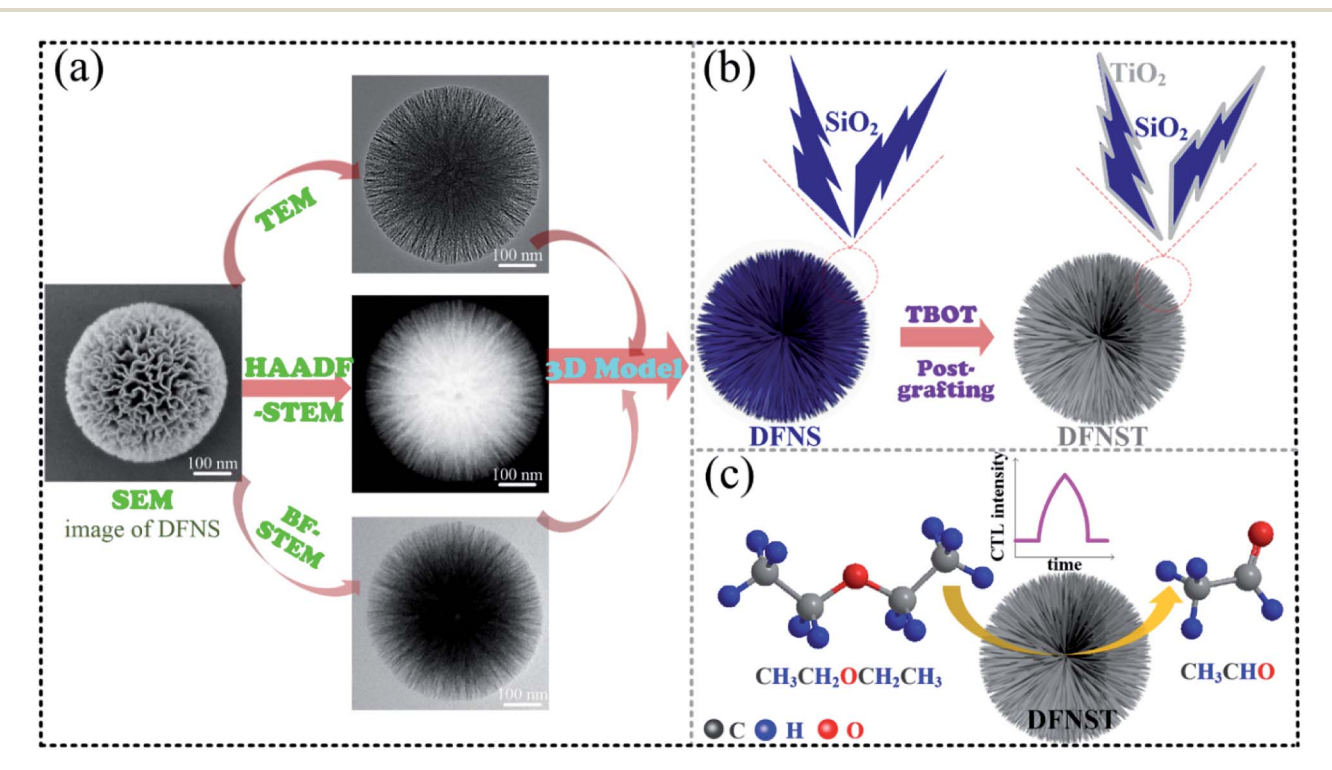


Fig. 1 (a) SEM, TEM, high-angle annular dark field STEM (HAADF-STEM), bright field STEM (BF-STEM) of a DFNS individual. (b) The 3D model of a DFNS and the schematic illustration of preparing DFNST by post-grafting TBOT onto DFNS with TiO₂ layer "coated". (c) Schematic illustration of DFNST-based CTL sensing material for the detection of diethyl ether.

RSC Advances

DFNST synthesis. DFNST was synthesized by the postgrafting approach with some modifications, on the basis of the ammonia-assisted solution-phase deposition technique.27 In a typical synthesis, DFNS (0.5 g) and anhydrous ethanol (100 mL) were placed in a round-bottomed flask with sufficient mixture (sonication for 30 min and stirring for 10 min). To the stirring solution, aqueous ammonia (1 mL, 25%) in 5 mL anhydrous ethanol was added dropwise over 10 min. After that, 2.5 mL TBOT with different amount in 5 mL anhydrous ethanol was then added dropwise at a speed of one liquid drop per ten seconds at RT. Then, the flask was connected to the vacuum system with sonication at 0 °C for 4 h. The reaction temperature was then boosted to 45 °C and kept for 20 h under continuous stirring. The resultant product was isolated by centrifugation, washed with abundant ethanol thrice, dried at 55 °C in an oven, and finally calcined at 750 °C for 5 h in air by a muffle furnace. In addition, the as-prepared pristine DFNST samples without post-calcination treatment are denoted as DFNST-ASP.

Characterization

Structural and physicochemical properties. Scanning electron microscopy (SEM) was carried out with a HITACHI-SU8010 field emission (Japan). Transmission electron microscopy (TEM) was conducted by a JEM-F200 (Japan) to obtain bright field (BF-STEM), high-angle annular dark field (HAADF-STEM), high resolution transmission electron microscopy (HRTEM), selected area electron diffraction (SAED), and TEM-mapping. Xray diffraction (XRD) patterns were redorded on a PANalytical X' Pert Pro X-ray diffractometer (Netherlands) with Cu Kα radiation. An autosorb-iQ2-MP analyzer (USA) was employed to measure N2 adsorption-desorption isotherms, and the data were dealt with BET analysis. A NEXUS-870 infrared spectrometer (USA) was utilized to record Fourier transform infrared spectroscopy (FT-IR). Raman spectra were recorded by a HORIBA LabRAM HR evolution with excitation at $\lambda = 532$ nm and an integration time of 100 s (France). XPS were performed on an ESCALAB 250Xi with Al Ka radiation (Thermo Fisher Scientific) and the binding energy scale was calibrated by hydrocarbon contamination with C 1s at 284.8 eV. The titanium content and silicon content were analyzed using a PerkinElmer 5300 ICP-OES instrument (PerkinElmer, USA), where each sample was predigested with a Milestone Ethos-1 microwave digester prior to measurement. The ultraviolet visible diffuse reflectance spectroscopy (UV-Vis-DRS) were measured with a UV-2550 UV-Vis spectrophotometer (Shimadzu, Japan).

CTL measurement. Diethyl ether was measured by an ultraweak luminescence analyzer via the DFNST-based CTL sensor. In general, 100 mg DFNST were uniformly coated on a cylindrical ceramic heater with the inner diameter of 0.5 cm and the length of 5.0 cm, which was inserted into the quartz tube with a diameter of 1.0 cm and a length of 7.0 cm. The operating temperature of 200 to 360 °C was controlled by a voltage controller. The flow rate was adjusted from 90 to 210 mL min⁻¹ by a precision flow meter. Different amount of diethyl ether gas of 5 mL (1 mM to 50 mM) was pumped into gasification chamber. The data integration time was set at one second per

count (1.0 s), and the detection limit was confirmed by the integration time of 0.5 s as well.

Results and discussion

SEM and TEM analysis

Fig. 2a displays SEM images of DFNS nanospheres with different magnifications. In order to observe the grafting process of TBOT onto DFNS, DFNST without calcination treatment (DFNST-ASP) were detected by SEM as shown in Fig. 2b. Even though TBOT precursor molecules hydrolyze to the sol-gel intermediate (mainly containing Ti-OH), the resultant products are still monodisperse without agglomeration and their surfaces keep smooth as well. Moreover, the nanopores are filled and packed obviously. The morphologies of these nanospheres greatly alter and the surfaces become rough upon calcining at 750 °C as exhibited in Fig. 2c. Spherical architectures are well preserved only with nanopores packed and decrescent. DFNS and DFNST samples with different TiO₂ loading were characterized by the ICP-OES technique and the results are summarized in Table 1. Fig. 2d displays TEM images of DFNS nanospheres with different magnifications. It is apparent that DFNS spheres possess the dendrimer-like structures with unique center-radial fibrous nanochannels. Fig. 2e shows TEM images of DFNST prepared by the post-grafting approach with calcination treatment. The dendritic structure becomes ambiguous and the center-radial state insensibly grades into solid shape from the outer to the inside. The nanochannels are filled with TiO₂ and become hard to be observed. The results confirm that 2.5 mL TBOT with Ti/Si molar ratio of 0.27 could be the ideal amount for DFNST of distinct dendritic fibrous morphology, in good agreement with SEM results.

Up to now, it is quite clear that DFNST can not only reserve representative dendritic fibrous architecture, but also load the sufficient TiO2 without destroying the dendritic fibrous morphology. Therefore, the sample was further explored by HR-TEM (Fig. 2f-h) and SAED (Fig. 2i). HR-TEM images manifest that some TiO₂ particles of ca. 10 nm disperse in DFNST channels (red circle). This observation demonstrates that part TBOT sol-gel coated on DFNS surface (Fig. 2b) thermally transforms into TiO₂ nanoparticles (Fig. 2f-h) under calcination procedure. As a consequence, smooth surfaces of DFNST-ASP without calcination (Fig. 2b, sol-gel) become rough (Fig. 2c, nanoparticles) after being heated at elevated temperature. The interplanar distances (d-spacings) of 0.35 nm from HR-TEM in Fig. 2h and the crystal planes of (101), (103), (200), (105), (213) from the SAED in Fig. 2i preliminary prove that the as-obtained TiO₂ is anatase with poly-crystal structure.

XRD, FT-IR, Raman, XPS, and N2 adsorption-desorption isotherms analyses

Fig. 3a shows XRD patterns of DFNS and DFNST specimens. Broad peak located at 22° between 15° and 30° corresponds to amorphous silica for DFNS.24,31,32 As for DFNST, this peak sharply lessened and characteristic peaks of anatase TiO2 show up including (101), (004), (200), (211), and (204). Combined with Paper

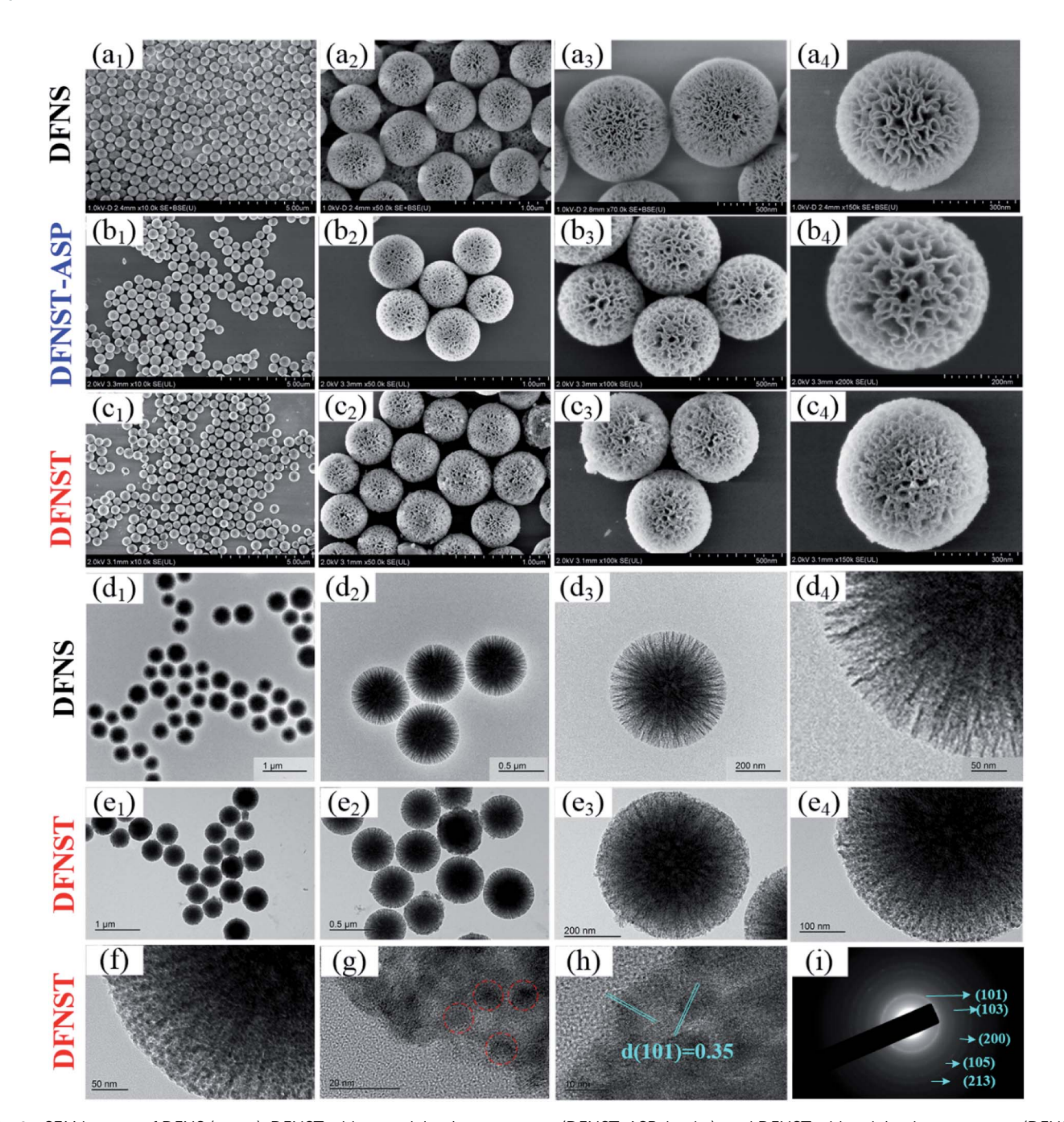


Fig. 2 SEM images of DFNS (a_1-a_4) , DFNST without calcination treatment (DFNST-ASP, b_1-b_4), and DFNST with calcination treatment (DFNST, c_1-c_4) under different magnifications. TEM images of DFNS (d_1-d_4) and DFNST (e_1-e_4) under different magnifications. HR-TEM images of DFNST under different magnifications (f-h) and the corresponding SAED result (i).

HR-TEM (Fig. 2f-h) and SAED (Fig. 2i) results, TiO₂ in DFNST can be fully confirmed to be anatase structure.

FT-IR spectrograms of DFNS and the as-prepared DFNST are exhibited in Fig. 3b. For DFNS reference, 1645 cm⁻¹, 1090 cm⁻¹, 963 cm⁻¹, and 810 cm⁻¹ can be ascribed to Si-O-Si, and H₂O,³² vibration absorptions of Si-OH,31 symmetrical stretching vibration of Si-O,33 respectively. The adsorbed H2O and Si-OH groups on the surfaces lead to the typical absorption of -OH group at 3430 cm⁻¹. As for DFNST, characteristic peaks of DFNS dwindle, indicating that these functional groups are covered by TiO₂ products or interact with TBOT. Characteristic flat broad peaks centered at 530 to 630 cm⁻¹ ascribe to vibration absorptions of Ti-O-Ti.34-36 The above results imply that Ti-OH groups originated from hydrolyzed TBOT condense with one another at the elevated temperature to generate Ti-O-Ti. More importantly, the peaks at about 960 cm⁻¹ that overlap with Si-OH and correspond to Si-O-Ti36,37 become easy to be observed from DFNS to DFNST, revealing that Ti-OH groups derived from hydrolyzed TBOT undergo hetero-condensation chemical reaction with Si-OH groups on DFNS substrates to produce Si-O-Ti

RSC Advances

Table 1 Chemical and textural properties of DFNS and DFNST

Sample	TBOT volume (mL)	$\mathrm{TiO_{2}}^{a}\left(\mathrm{wt\%}\right)$	SiO_2^a (wt%)	Ti/Si ^b (molar ratio)	$S_{\rm BET}$ (m ² g ⁻¹)	$V_{\rm P}$ (cm ³ g ⁻¹)
DFNS	0	0	80.27	0	421.374	1.314
DFNST	2.5	21.44	60.42	0.27	310.514	0.737

 $[^]a$ Measured by ICP-OES analysis. b Calculated by ICP-OES result; S_{BET} stands for BET surface area; V_{P} is pore volume.

cross-linked structures. Raman tests of the as-prepared DFNST are also conducted to further ascertain TiO2 crystal structure (Fig. 3c). Typical anatase peaks of $E_{\rm g},~B_{\rm 1g},$ and $A_{\rm 1g}$ + $B_{\rm 1g}$ are detected and located at around 140 (630), 380, and 500 cm⁻¹, respectively.38-40

The prominently intense low frequency mode at 140 cm⁻¹ can be attributed to O-Ti-O bending vibration within coordinated TiO2 octahedra. XPS survey spectra of DFNST (Fig. 3d)

reveals that Si 2p, O 1s, and Ti 2p collectively exist on its surface, except for C 1s contamination. The corresponding highresolution XPS spectra of Si 2p, O 1s, and Ti 2p are presented in Fig. 3e-g. De-convolution of O 1s produces three peaks and can be ascribed to Ti-O-Ti at 530.32 eV, Si-O-Ti at 532.49 eV, and Si-O-Si at 533.62 eV, respectively. 41,42 This result coincides with the previously reported one that hetero-condensation of Si-O-Ti takes place during DFNST formation.43 Ti 2p XPS

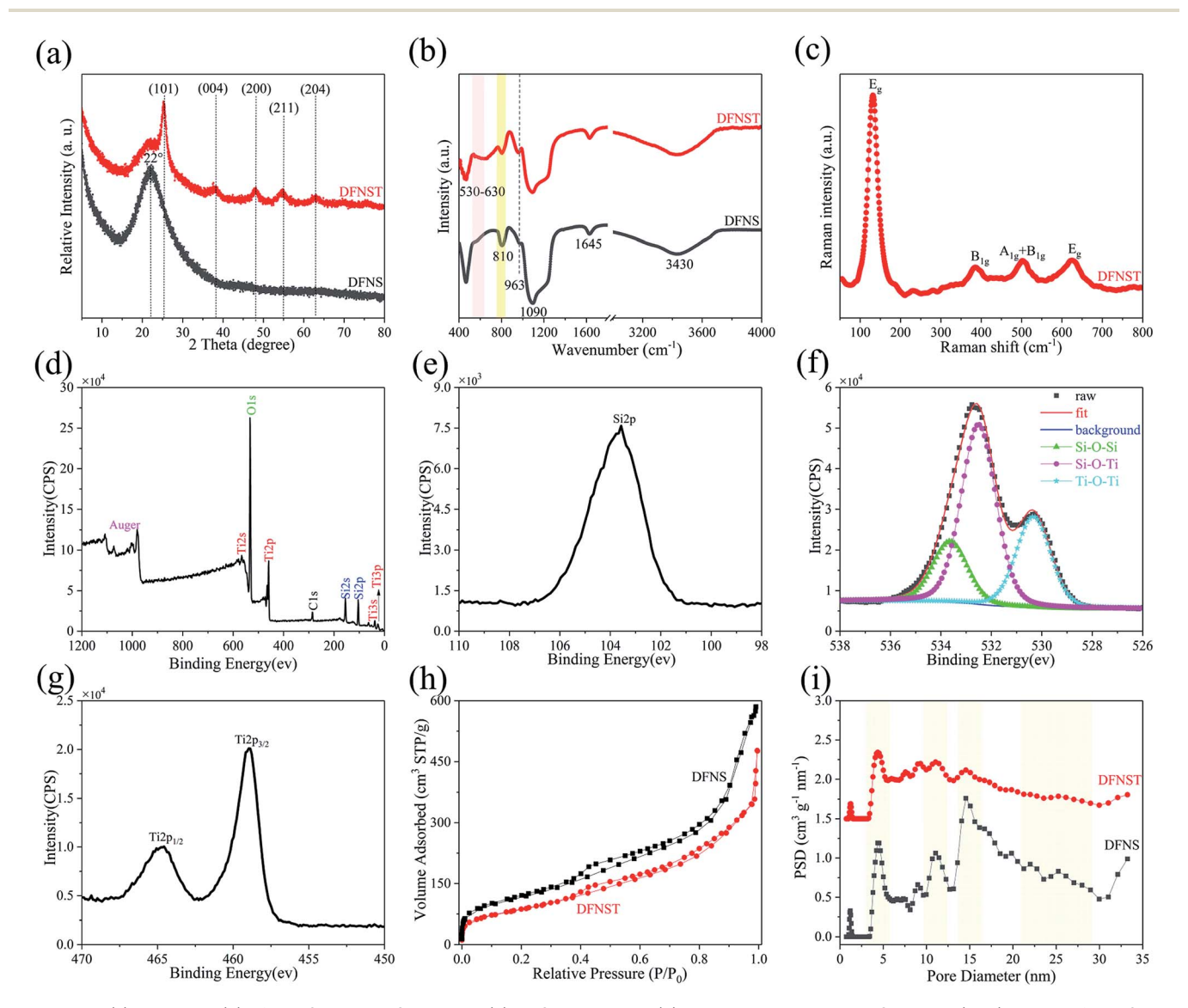


Fig. 3 XRD (a) and FT-IR (b) of DFNS and DFNST. Raman (c), XPS survey scan (d), and high-resolution XPS spectra (e-g) curves of DFNST. N₂ adsorption-desorption isotherms (h) and the corresponding pore size distributions (i) of DFNS and DFNST.

spectra demonstrates the typical doublet peaks of Ti 2p_{3/2} at 458.97 eV and Ti 2p_{1/2} at 464.57 eV.42 The N₂ adsorptiondesorption isotherms and the corresponding pore size distributions of DFNS and the as-prepared DFNST are shown in Fig. 3h and i, respectively. All samples have similar IV characters of typical H₃ hysteresis loops in their isotherms. It is well-known that type H₃ loop usually appears with aggregates of plate-like particles that evolve into slit-shaped pores,44 here in correspondence with the nanochannels of the bulks. The pore size of DFNS exhibits four evident wide distributions at ca. 4, 11, 15, and 25 nm, which could be various nanopores in DFNS as verified by SEM, TEM, and our previous reports.30 For DFNST sample, the peaks become weaker and even vanish. The corresponding pore volume (V_P) and BET surface area (S_{BET}) are listed in Table 1. DFNS nanospheres synthesized without TBOT have the maximum S_{BET} and V_{P} . S_{BET} and V_{P} greatly decrease as TBOT was added, nearly three fourths of DFNS reference. Based on the above SEM, TEM, ICP-OES, and N₂ adsorption-desorption results, it can be concluded that DFNST could be the ideal target products which load sufficient anatase TiO2 without damaging the particular dendritic fibrous textures.

Optimization of CTL conditions and the sensor's stability

To gain the optimal working parameters (conditions) for the detection of ether, optimization processes for excellent CTL ability of DFNST were performed where the wavelength of CTL emission, the working temperature, and the flow rate of gas carrier were successively probed into (Fig. 4a-c). Eight wavelengths of CTL emission were investigated as displayed in Fig. 4a and S1† (the original data), including 400, 425, 440, 460, 490, 555, 575 and 620 nm. It can be clearly seen that CTL intensity boosts with the increase of filter wavelength below 440 nm and decreases sharply above 440 nm. The maximal CTL intensity locates at 440 nm which was selected as the optimal detection wavelength for the subsequent studies. To our excitement, nearly all noise signal can be eliminated with the bandpass filter at 440 nm, as verified in Fig. S2.† In addition, the CTL intensity is very strong under this situation with the value of about 2×10^5 count. Hence, the bandpass filter at 440 nm was utilized throughout the following experiments without discussing the signal/noise (S/N) ratio.2 CTL intensity of DFNST towards working temperatures were measured and the results were demonstrated in Fig. 4b and S3† (the original data). On the whole, the intensity increases monotonically from 200 to 360 °C. When the working temperatures is less than 240 °C, the corresponding CTL intensity is very weak. When the working temperatures outweigh 260 °C, the corresponding CTL intensity greatly increase with a gradient of K. However, the increase trend decreases as the working temperatures reaches 300 °C with a gradient of K'. Therefore, 280 °C was considered as the optimal detection temperature for the subsequent researches (K' < K). Fig. 4c and S4† (the original data) illustrate the CTL intensity at different rate of 90 to 300 mL min⁻¹ under the optimized working temperature of 280 °C and the wavelength of 440 nm. It is clear that the maximal CTL intensity locates at 210 mL min⁻¹ which was selected as the optimal rate for the

subsequent studies. The CTL intensity begins to decrease as the flow rate is greater than 210 mL min⁻¹, which might be aroused by insufficient reaction time between DFNST and ether. Under the optimum experimental conditions (440 nm, 280 °C, and 210 mL min⁻¹), the curve of CTL intensity versus diethyl ether concentration was plotted as shown in Fig. 4d and S5.† The intensity is proportional to the concentration in a range of 2.0 to 40 mM (Fig. 4e). The liner equation can be y = 10183x - 25288with R^2 of 0.9963, where y and x are CTL intensity and ether concentration, respectively. The detection limit of diethyl ether (S/N \approx 3) is 1.55 mM which was validated both in the data integration time of 1.0 s and 0.5 s, as exhibited in Fig. 4f. The stability of the as-prepared DFNST-based sensor was conducted by persistently injecting 20 mM ether for seven rounds. The relative standard deviation (RSD) was 2.47%, indicative of the sensor's highly stability (Fig. 4g). The as-prepared DFNST-based sensor suffered about 200 tests under different experiment conditions for the optimization of CTL conditions, the exploration of CTL intensity versus diethyl ether concentration as well as the detection limit, RSD determination, and VOCs selectivity (displayed later). The color of the fresh DFNST without any test as the sensing material is white and becomes yellow after all these tests (Fig. 4h). However, the chemical composition of the utilized DFNST remains unchanged as indicated by XRD result in Fig. S7.† SEM images of the final products were also characterized as photographed in Fig. 4i. It is clear to be observed that the morphology and the structure of the final DFNST are highly identical with the pristine ones (Fig. 2c), revealing the outstanding stability of this sensing material.

The selectivity of DFNST-based CTL sensor and the plausible mechanism

The CTL spectra of different VOCs (herein, including ether, acetone, ethyl acetate, butanol, ethyl alcohol, acetaldehyde, formaldehyde, methanol, and acetic acid) were measured using the DFNST-based sensor without or with the bandpass filter at 440 nm. As shown in Fig. 5a and S6,† diethyl ether, acetone, ethyl acetate, and butanol exhibit CTL signals of different relative intensities without the 440 nm bandpass filter, revealing that diethyl ether cannot be discriminated over these VOCs under this circumstance. Oppositely, CTL signals of diethyl ether, acetone, ethyl acetate, and butanol are largely prevented with the bandpass filter. Nevertheless, ether shows an apparent CTL signal than the other three. The selective detection of ether could be realized easily, proving that the DFNST-based sensor is sensitive and effective. It is well-known that the high selectivity can be primarily ascribed to the various VOCs reaction intermediates. Previous investigations have testified that the emitter from ether-TiO2 CTL sensors was excited-state CH₃CHO*. Diethyl ether transformed into CO₂ byproducts and acetaldehyde in the end.2,9 BTB indicator and the saturated Ca(OH)₂ solution were applied to demonstrate the yield of CO_2 in Fig. 5b and c. BTB solution was blue (I, pH \geq 8), and turned into the blue-green (II) as the blank air carrier was injected because of the existence of CO2 in air. An obvious change happened and the color became green (III, pH = 6-7)

RSC Advances Paper

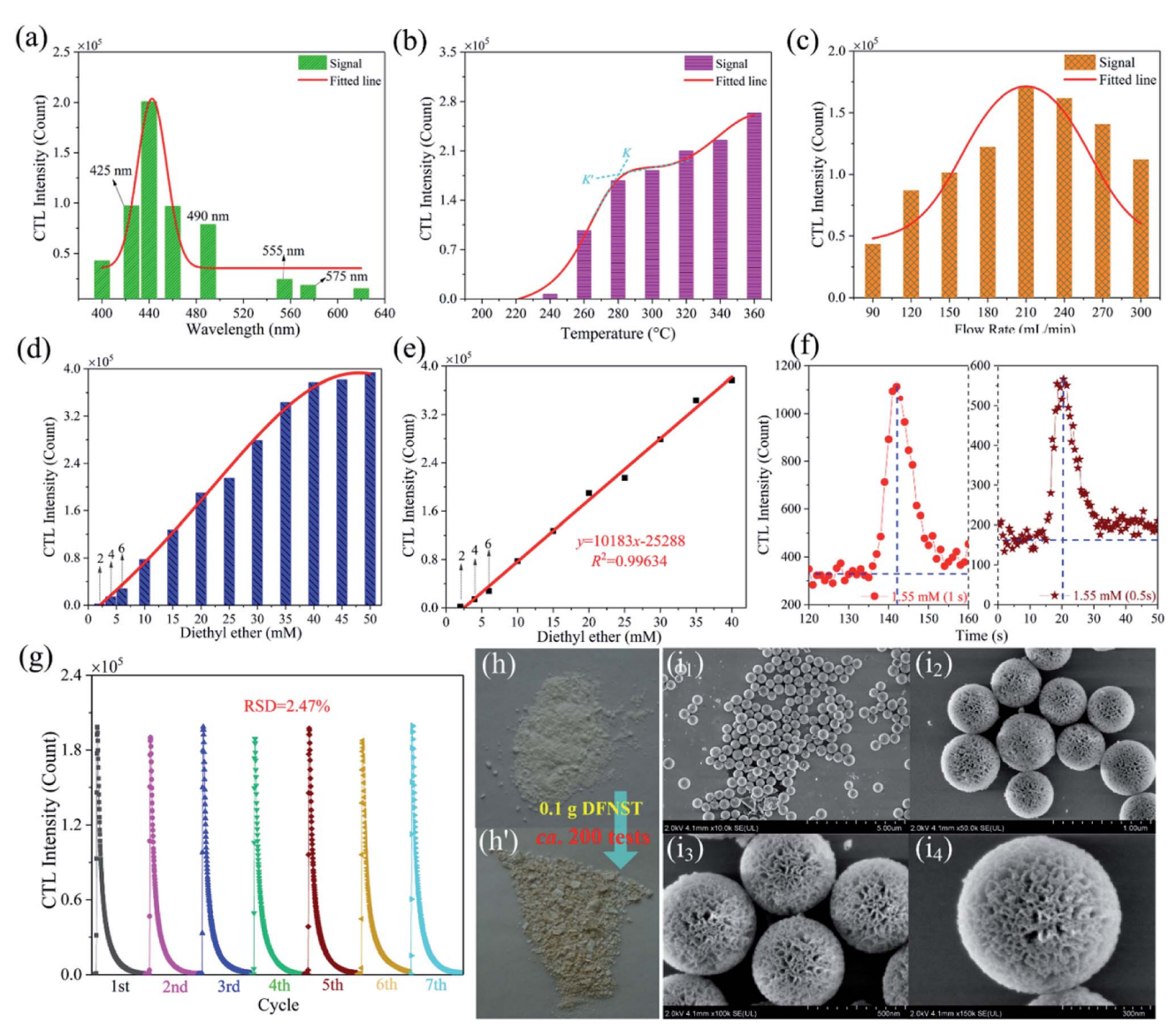


Fig. 4 The CTL intensity of ether on DFNST at different wavelengths with working temperature of 280 °C, air flow rate of 210 mL min⁻¹, and diethyl ether concentration of 20 mM (a). The CTL intensity of diethyl ether on DFNST at different working temperatures with air flow rate of 210 mL min⁻¹ and diethyl ether concentration of 20 mM under 440 nm wavelength (b). The CTL intensity of ether on DFNST at different air flow rates with working temperature of 280 °C and ether concentration of 20 mM at 440 nm wavelength (c). The plot of CTL intensity *versus* different diethyl ether concentration (d), the corresponding calibration curve (e), the detection limit of diethyl ether (f), and the relative standard deviation of DFNST (g) under the optimum experimental conditions. The photographs of the pristine DFNST without any test and the final DFNST with all tests (h). SEM images of the final DFNST with all tests under different magnifications (i).

owing to the generated plentiful CO_2 as the tail gas was injected. In the same way, saturated $Ca(OH)_2$ solution changed from clear (Fig. 5c(I')) to slightly turbid (Fig. 5c(II')) and further to severely turbid (Fig. 5c(III')) due to the increase of CO_2 amount. Based on the above results, the controllable selective ether detection can be facilely achieved by means of a 440 nm bandpass filter under ambient condition. For the practical application of the as-prepared DFNST-based sensor, it can be utilized to detect trace amount of diethyl ether in medicines or cosmetics like perfumes where the diethyl ether concentrations are about 7.0 mM² and the related investigations are being carried out by us.

In order to explore CTL mechanism of the sensor, diffuse reflectance UV-Vis spectral analysis was carried out to detect the presence of Ti species in DFNST and their coordination states. No absorption band exists for DFNS as indicated by an almost flat curve shown in Fig. 5d. As for hybrid product, a broad absorption band located at 200 to 370 nm is easy to be observed and commonly can be divided into two individuals: the weak band at 202–230 nm and another one at 250–370 nm, respectively. The former can be ligand to metal charge transfer (LMCT) from O to Ti with tetrahedral titanium in TiO_2 where SiO-Ti bonds develop; the latter also can be ascribed to LMCT but with Ti atoms in an octahedral where Ti-O-Ti bonds occur. The

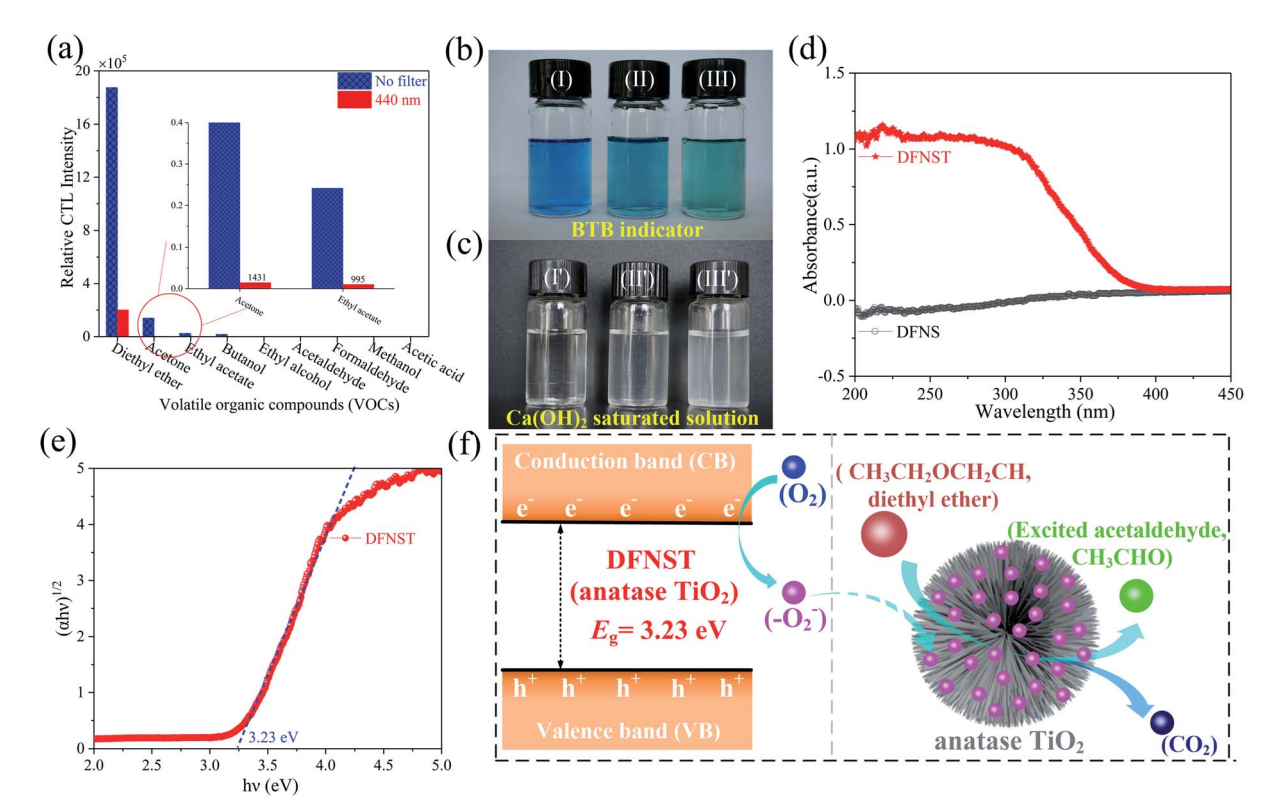


Fig. 5 The CTL spectra of different VOCs on DFNST-based sensor without or with the bandpass filter at 440 nm (a). The color change of BTB (b) and saturated $Ca(OH)_2$ solutions (c) by injecting nothing (I), the blank air carrier (II), and the tail gas (III). UV-Vis-DRS spectra (d) and band gap E_g (e) of DFNST. The plausible CTL mechanism of diethyl ether on DFNST-based sensor (f).

above results imply that partial Ti–OH groups heterogeneously condense with Si–OH groups in DFNS for the formation of Si–O–Ti and some other Ti–OH groups condense with one another at the elevated temperature for the formation of Ti–O–Ti, in good agreement with FT-IR and XPS results. Furthermore, UV-Vis-DRS was analyzed using Tauc plot to explore the band gap of DFNST (Fig. 5e). An indirect band gap exists in the hybrid material and the band gap value equals to 3.23 eV that corresponds to crystalline TiO₂ of anatase structure.^{23,40}

Based on these results, the mechanism of diethyl ether on DFNST-based CTL sensor is proposed in Fig. 5f. Firstly, anatase TiO_2 ($E_g=3.23$ eV) in DFNST can be motivated to generate hole (h⁺) and free electron (e⁻) at 280 °C (eqn (1)). Secondly, O_2 adsorbed on the surfaces of DFNST nanochannels can be excited to generate oxygen activity species O_2^- with an electron from anatase TiO_2 (eqn (2)). The as-produced O_2^- with the high capability of oxidization react with diethyl ether molecules that also adsorbed on the surface of DFNST nanochannels, giving rise to the excited-state intermediates of CH_3CHO^* and CO_2^* (eqn (3)). Finally, the CH_3CHO^* and CO_2^* return to ground-state of CH_3CHO and CO_2 , accompanied with luminescence phenomenon (eqn (4) and (5)). The high response can be attributed to unique architectural texture of DFNST.

$$DFNST \rightarrow DFNST (e^{-}) + DFNST (h^{+})$$
 (1)

$$O_2^- + e^- \to O_2^-$$
 (2)

$$(C_2H_5)_2O + O_2^- \rightarrow CH_3CHO^* + CO_2^* + O_2$$
 (3)

$$CH_3CHO^* \rightarrow CH_3CHO + e^- + h\nu$$
 (4)

$$CO_2^* \rightarrow CO_2 + e^- + hv \tag{5}$$

Conclusions

In summary, we have synthesized dendritic fibrous nano-silica & titania (DFNST) hybrids as novel sensing materials to successfully fabricate DFNST-based cataluminescence sensor for ether detection. The as-prepared sensor possesses high selectivity by locating detection position with one 440 nm bandpass filter. Ether could be easily monitored in the range of 2.0–40 mM with a detection limit of 1.55 mM under the optimal conditions. The DFNST-based CTL sensor is stable and durable without damaging the morphology and activity of the sensing material after about 200 tests. It is expected that this novel sensing material and the corresponding CTL sensor will be significant for the detection of ether in actual application.

Conflicts of interest

There are no conflicts to declare.

Acknowledgements

This work was supported by Natural Science Basic Research Plan in Shaanxi Province of China (No. 2019JQ-104), Doctoral Research Program of Yan'an University (No. YDBK2017-39), the Research Program of Yan'an University (No. YDQ2018-14), Shaanxi Province Training Program of Innovation and Entrepreneurship for Undergraduates (No. 201820042), Innovation Project of Graduate Education from Yan'an University (No. YCX201822).

Notes and references

- 1 H. Lin, M. Jang and K. S. Suslick, J. Am. Chem. Soc., 2011, 133, 16786–16789.
- 2 L. Zhang, S. Wang, Z. Yuan and C. Lu, Sens. Actuators, B, 2016, 230, 242-249.
- 3 H. Xu, Q. Li, L. Zhang, B. Zeng, D. Deng and Y. Lv, *Anal. Chem.*, 2016, **88**, 8137–8144.
- 4 L. Li, C. Wei, H. Song, Y. Yang, Y. Xue, D. Deng and Y. Lv, *Anal. Chem.*, 2019, **91**, 13158–13164.
- 5 H. Song, L. Zhang, C. He, Y. Qu, Y. Tian and Y. Lv, J. Mater. Chem., 2011, 21, 5972–5977.
- 6 X. Wang, N. Na, S. Zhang, Y. Wu and X. Zhang, *J. Am. Chem. Soc.*, 2007, **129**, 6062–6063.
- 7 J. Hu, L. Zhang, H. Song, J. Hu and Y. Lv, Anal. Chem., 2019, 91, 4860–4867.
- 8 G. Shi, B. Sun, Z. Jin, J. Liu and M. Li, *Sens. Actuators, B*, 2012, **171**, 699–704.
- 9 Y. Zhen, H. Zhang, F. Fu and Y. Zhang, *J. Mater. Sci.: Mater. Electron.*, 2019, **30**, 3722–3728.
- 10 Y. Wang, X. Du, Z. Liu, S. Shi and H. Lv, *J. Mater. Chem. A*, 2019, 7, 5111–5152.
- 11 A. Maity, R. Belgamwar and V. Polshettiwar, *Nat. Protoc.*, 2019, **14**, 2177–2204.
- 12 A. Maity, S. Mujumdar and V. Polshettiwar, ACS Appl. Mater. Interfaces, 2018, 10, 23392–23398.
- 13 Y. Wang, Y. Wang, X. Li, J. Li, L. Su, X. Zhang and X. Du, *ACS Sustainable Chem. Eng.*, 2018, **6**, 14071–14081.
- 14 W. Byoun, S. Jung, N. M. Tran and H. Yoo, *ChemistryOpen*, 2018, 7, 349–355.
- 15 S. Li, X. Jiang, H. Sun, S. He, L. Zhang and L. Shao, *J. Membr. Sci.*, 2019, **586**, 185–191.
- 16 P. Yang, Q. Liu, J. Liu, R. Chen, R. Li, X. Bai and J. Wang, *J. Hazard. Mater.*, 2019, **363**, 248–257.
- 17 V. Polshettiwar, D. Cha, X. Zhang and M. B. Jean, *Angew. Chem., Int. Ed.*, 2010, **49**, 9652–9656.
- 18 V. Polshettiwar, J. Thivolle-Cazat, M. Taoufik, F. Stoffelbach and S. Norsic, *Angew. Chem., Int. Ed.*, 2011, **50**, 2747–2751.
- 19 A. Fihri, D. Cha, M. Bouhrara, N. Almana and V. Polshettiwar, *ChemSusChem*, 2012, 5, 85–89.

- 20 M. Bouhrara, C. Ranga, A. Fihri, R. R. Shaikh, P. Sarawade, A. H. Emwas, M. N. Hedhili and V. Polshettiwar, ACS Sustainable Chem. Eng., 2013, 1, 1192–1199.
- 21 X. Huang, Z. Tao, J. C. Praskavich, A. Goswami, J. F. Al-Sharab, T. Minko, V. Polshettiwar and T. Asefa, *Langmuir*, 2014, 30, 10886–10898.
- 22 Z. S. Qureshi, P. B. Sarawade, M. Albert, V. D'Elia, M. N. Hedhili and K. Köhler, *ChemCatChem*, 2015, 7, 635–642.
- 23 R. Singh, R. Bapat, L. Qin, H. Feng and V. Polshettiwar, *ACS Catal.*, 2016, **6**, 2770–2784.
- 24 Z. S. Qureshi, P. B. Sarawade, I. Hussain, H. Zhu, H. Al-Johani, D. H. Anjum, M. N. Hedhili, N. Maity, V. D'Elia and J. M. Basset, *ChemCatChem*, 2016, 8, 1671–1678.
- 25 B. Singh and V. Polshettiwar, J. Mater. Chem. A, 2016, 4, 7005–7019.
- 26 S. M. Saadati and S. M. Sadeghzadeh, Catal. Lett., 2018, 148, 1692–1702.
- 27 N. Bayal, R. Singh and V. Polshettiwar, *ChemSusChem*, 2017, 10, 2182–2191.
- 28 S. Kundu and V. Polshettiwar, *ChemPhotoChem*, 2018, 2, 796–800.
- 29 T. Qian, X. Yin, J. Li, H. E. Nian, H. Xu, Y. Deng and X. Wang, J. Mater. Sci. Technol., 2017, 33, 1314–1322.
- 30 Y. Wang, K. Hu, J. He and Y. Zhang, *RSC Adv.*, 2019, **9**, 24783–24790.
- 31 H. Yang, S. Li, X. Zhang, X. Wang and J. Ma, *J. Mater. Chem. A*, 2014, 2, 12060–12067.
- 32 S. M. Sadeghzadeh, Green Chem., 2015, 17, 3059-3066.
- 33 Z. Sun, H. Li, D. Guo, J. Sun, G. Cui, Y. Liu, Y. Tian and S. Yan, *J. Mater. Chem. C*, 2015, 3, 4713–4722.
- 34 A. Nyquist and R. O. Kagel, *Infrared Spectra of Inorganic Compounds (3800-45 cm*⁻¹), Academic Press, New York, 1971.
- 35 Z. Li, B. Hou, Y. Xu, D. Wu and Y. Sun, *J. Colloid Interface Sci.*, 2005, **288**, 149–154.
- 36 J. Ren, Z. Li, S. Liu, Y. Xing and K. Xie, *Catal. Lett.*, 2008, **124**, 185–194.
- 37 C. X. C. Lin, C. Xu, Y. Yang, C. Lei, H. Zhang and C. Yu, *New J. Chem.*, 2017, **41**, 8754–8760.
- 38 D. Dastan, Appl. Phys. A: Mater. Sci. Process., 2017, 123, 699.
- 39 Y. Lian, W. Zhu, W. Yao, H. Yi, Z. Hu, T. Duan, W. Cheng, X. Wei and G. Hu, *New J. Chem.*, 2017, **41**, 4212–4219.
- 40 H. Tang, K. Prasad, R. Sanjines, P. E. Schmid and F. Levy, J. Appl. Phys., 1998, 75, 2042–2047.
- 41 H.-T. Lu, S.-L. Huang, I.-H. Tseng, Y.-K. Lin and M.-H. Tsai, *J. Appl. Polym. Sci.*, 2013, **127**, 145–153.
- 42 S. Wang, Y. Shi and X. Ma, *Microporous Mesoporous Mater.*, 2012, **156**, 22–28.
- 43 R. Singh, N. Bayal, A. Maity, D. J. Pradeep, J. Trébosc, P. K. Madhu, O. Lafon and V. Polshettiwar, *ChemNanoMat*, 2018, 4, 1–10.
- 44 K. S. W. Sing, Pure Appl. Chem., 1985, 57, 603-619.